Electron spin and momentum lifetimes in two-dimensional Si accumulation channels: Demonstration of Schottky-barrier spin metal-oxide-semiconductor field-effect transistors at room temperature

Shoichi Sato,[1] Mitsuki Ichihara,[1] Masaaki Tanaka,[1,2] and Ryosho Nakane[1,3]

[1]*Department of Electrical Engineering and Information Systems, The University of Tokyo, 7-3-1 Hongo, Bunkyo-ku, Tokyo 113-8656, Japan*

[2]*Center for Spintronics Research Network (CSRN), The University of Tokyo, 7-3-1 Hongo, Bunkyo-ku, Tokyo 113-8656, Japan*

[3]*Institute for Innovation in International Engineering Education, The University of Tokyo, 7-3-1 Hongo, Bunkyo-ku, Tokyo 113-8656, Japan*

(Received 29 December 2018; revised manuscript received 10 March 2019; published 1 April 2019)

We have investigated the electron spin lifetime τ_S and momentum lifetime τ in a two-dimensional (2D) accumulation channel of Schottky-barrier spin metal-oxide-semiconductor field-effect transistors (spin MOSFETs). The spin MOSFETs examined in this study have Fe/Mg/MgO/Si Schottky-tunnel junctions at the source/drain and a 15-nm-thick nondegenerated Si channel with a phosphorus donor doping concentration N_D of $1 \times 10^{17}\,\mathrm{cm}^{-3}$. We estimated τ and the electron diffusion coefficient D_e in the 2D accumulation channel from experimental results of a Hall-bar-type MOSFET device and self-consistent calculations using Poisson's and Schrödinger's equations. The spin MOSFETs with various channel lengths L_{ch} ($= 0.3-10\,\mu\mathrm{m}$) exhibited transistor characteristics with a high on/off ratio of $\sim 10^6$ as well as clear spin-valve signals at 295 K. From the spin-valve signals measured with various gate electric fields ($2-5\,\mathrm{MV/cm}$), τ_S and the electron spin diffusion length λ_S were estimated. We found that the spin-flip rate per one momentum scattering event τ/τ_S is $\sim 1/14\,000$, which is almost unchanged by the gate electric field. The proportionality between τ_S and τ indicates that the Elliott-Yafet mechanism is dominant in the Si 2D electron accumulation channel, and that the spin-flip rate per one phonon scattering event and that per one surface roughness scattering event are the same. Based on the Elliott-Yafet theory, there is a possibility that the spin-orbit coupling in the Si 2D accumulation channel is almost twice as strong as that in bulk Si materials.

DOI: 10.1103/PhysRevB.99.165301

I. INTRODUCTION

Recently, Si-based spin metal-oxide-semiconductor field-effect transistors (spin MOSFETs) have attracted much attention, since they have a potential capability to create next-generation electronics by adding their functionalities of nonvolatile memory, storage, and reconfigurable transistor characteristics [1–3] to the well-established complementary metal-oxide-semiconductor (CMOS) technology. A basic spin MOSFET has an ordinary MOSFET structure with a Si channel, but its source (S) and drain (D) contacts are replaced by ferromagnetic materials or ferromagnetic multilayered structures. The S/D contacts act as a spin injector/detector of spin-polarized electrons into/from the Si channel, respectively, to realize magnetoresistance (MR) by the spin-dependent electron transport through the two-dimensional (2D) electron inversion or accumulation channel. As a result, the transistor characteristics of a spin MOSFET can be changed by the magnetization configurations (parallel/antiparallel) between the S and D contacts. For practical use, the modulation ratio of the output current, which is characterized by the MR ratio, should be large enough. In this respect, Si is a promising channel material, since a long electron spin lifetime τ_S (a long electron spin diffusion length λ_S) of electrons is expected due to its weak spin-orbit coupling (SOC), which is strongly required to obtain a large MR ratio.

Motivated by the background described above, there have been many experimental studies on Si-based spintronics so far, whose topics are mainly divided into two parts: (i) spin injection/extraction into/from Si and (ii) spin-dependent transport via a Si channel. Many experimental studies focused on the spin injectors/extractors using ferromagnetic metals (FMs) to optimize the FM/Si junction properties for highly efficient spin injection/extraction into/from a Si channel [4–6]. Although some guidelines for high-performance spin injectors/extractors have been revealed, the junction resistance used in most of the studies is too high to obtain a large MR ratio when it is applied to the S and D contacts in a device with a Si channel. Thus, regarding spin injection/extraction into/from Si, we need to further clarify the physics and develop the junction process technology.

On the other hand, there have been a few experimental studies on the spin-dependent transport through a Si 2D electron inversion/accumulation channel [7–12]. In a recent successful demonstration of a Si-based spin MOSFET with a phosphorus-doped Si 2D electron accumulation channel [11], a noteworthy result was that λ_S in their 2D electron accumulation channel was $\sim 1\,\mu\mathrm{m}$ at room temperature, which is significantly shorter than that ($\sim 3\,\mu\mathrm{m}$) in a bulk Si material with a similar phosphorus donor doping concentration $N_D \sim 2 \times 10^{18}\,\mathrm{cm}^{-3}$ [11]. Another study also reported a short spin lifetime $\tau_S \sim 1\,\mathrm{ns}$ in a 2D electron inversion channel with

an undoped Si [12]. However, these two studies [11,12] did not quantitatively reveal the reason why λ_S or τ_S becomes shorter in the Si 2D electron inversion/accumulation channel than in bulk Si materials. Based on the Elliott-Yafet theory [13–15], spin flip occurs in a part of electron momentum scatterings; namely, there is a relation between τ_S and electron momentum lifetime τ. Theoretically, in a Si 2D electron inversion/accumulation channel, τ is determined by three scattering mechanisms; the intravalley acoustic phonon scattering, the intervalley optical phonon scattering, and the surface roughness scattering [16]. Selberherr's group theoretically calculated τ_S in a Si thin channel taking into account the phonon scattering and surface roughness scattering, and showed that the ratio τ_S/τ is almost constant in a wide temperature range (50–500 K) and τ_S/τ can be enhanced by an in-plane biaxial strain [17,18]. To further understand the spin-dependent electron transport through a Si 2D electron inversion/accumulation channel, it is very important to clarify the relation between τ_S and τ, and thus its quantitative analysis is needed by the combination of both experimental and theoretical investigations.

In the field of Si-based ordinary MOSFETs, the quantitative analysis method of a Si 2D electron inversion/accumulation channel has been almost established [19–27]. By using both experimental results and self-consistent calculations, we can obtain the momentum lifetime concerning each scattering process, from which the total τ value can be estimated by Matthiessen's rule. A remarkable feature of a Si 2D electron inversion/accumulation channel is that the dominant momentum scattering mechanism can be changed by the gate electric field that is applied perpendicularly to the channel [16]. Thus, if this quantitative method is used for the analysis of spin MOSFETs, we can reveal the relation between τ_S and τ in a Si 2D electron inversion/accumulation channel as a function of the gate electric field, and furthermore, we can clarify which momentum scattering mechanism dominates the spin relaxation.

In this study, we experimentally investigate the spin injection/extraction and spin transport in a Si 2D electron accumulation channel in Schottky-barrier (SB) spin MOSFETs at room temperature, and clarify the relation between τ_S and τ in the channel. In Sec. II, we prepare a Hall-bar-type MOSFET and reveal important physical parameters as a function of the effective gate electric field from both experiments and self-consistent calculations, in which the parameters to be estimated are the electron mobility μ, the channel sheet resistance R_{ch}, the electron diffusion coefficient D_e, and the electron momentum lifetimes for the intravalley acoustic phonon scattering τ_{ac}, the intervalley optical phonon scattering τ_{op}, and the surface roughness scattering τ_{sr}. Although τ_{sr} is caused by the roughness of the Si/SiO_2 interface, we call it "surface" roughness scattering following the previous papers. In Sec. III, we prepare spin MOSFETs with various channel lengths L_{ch} ($= 0.3-10\,\mu$m) and measure the spin-dependent transport. In Sec. IV, we obtain an almost constant τ/τ_S ratio ($\sim 1/14\,000$), which is independent of the dominant scattering process, by analyzing the magnetoresistance for various gate electric fields and L_{ch}. In Sec. V, we discuss the origin of the constant τ/τ_S ratio. In Sec. VI, we make concluding remarks and address future issues.

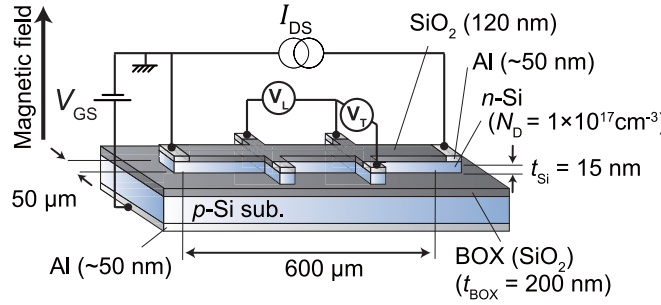

FIG. 1. Schematic illustration of a Hall-bar-type metal-oxide-semiconductor field-effect transistor (MOSFET) prepared on a silicon-on-insulator (SOI) substrate, where the channel thickness t_{Si} is 15 nm; the channel length and width are 600 and 50 μm, respectively; the phosphorus donor doping concentration N_D in the channel is 1×10^{17} cm^{-3}; and the thickness of a buried oxide (SiO_2) layer t_{BOX} for the back gate is 200 nm. The measurement setup is also shown, where a constant drain-source current I_{DS} and a constant gate-source voltage V_{GS} were applied and the longitudinal and transverse voltages V_L and V_T, respectively, were measured while a sweeping magnetic field was applied perpendicular to the substrate plane.

II. ELECTRON TRANSPORT PROPERTIES IN A Si TWO-DIMENSIONAL ACCUMULATION CHANNEL

To investigate the relation between the electron momentum lifetime τ and electron spin lifetime τ_S, at first we characterize the electron transport properties through a Si 2D electron accumulation channel. The results obtained in this section will be used for the characterizations and analyses of spin MOSFETs in the later sections. Figure 1 shows a schematic illustration of a back-gated Hall-bar-type device with a channel length/width $= 600\,\mu$m$/50\,\mu$m, which was prepared by the following procedure. We used a (001)-oriented silicon-on-insulator (SOI) substrate consisting of (from top to bottom) a 100-nm-thick Si layer, a buried silicon dioxide (BOX) layer with a thickness $t_{BOX} = 200$ nm, and a lightly doped p-type Si substrate with a boron accepter doping concentration of $\sim 10^{15}$ cm^{-3}. First, the top 100-nm-thick Si layer was doped with phosphorus donor atoms using a spin-coated phosphorus glass and thermal diffusion at 750 °C. The phosphorus donor doping profile was uniform and the concentration N_D was 1×10^{17} cm^{-3} that was calibrated by secondary ion mass spectroscopy (SIMS) analysis. After removal of the phosphorus glass by buffered HF (BHF), the substrate was thermally oxidized at 1050 °C with dry oxygen gas to form a 210-nm-thick surface SiO_2 layer and a 15-nm-thick Si channel layer. Hereafter, this substrate is called "SiO_2/SOI substrate." Next, electrode contact areas were defined by opening contact holes in a photoresist layer on the top, and then the surface SiO_2 was etched with BHF so that the SiO_2 thickness of these areas became $\sim$20 nm. This thinned SiO_2 layer can avoid contamination of the Si surface by the photoresist during removal. After removal of the photoresist, the substrate was cleaned by a $H_2SO_4 + H_2O_2$ solution, followed by flowing de-ionized pure (DI) water. Then, the Si surfaces of the contact areas were opened by dipping the whole substrate into BHF, and a 100-nm-thick Al layer was formed on the top by thermal evaporation. At this stage, a 120-nm-thick SiO_2 layer remained except

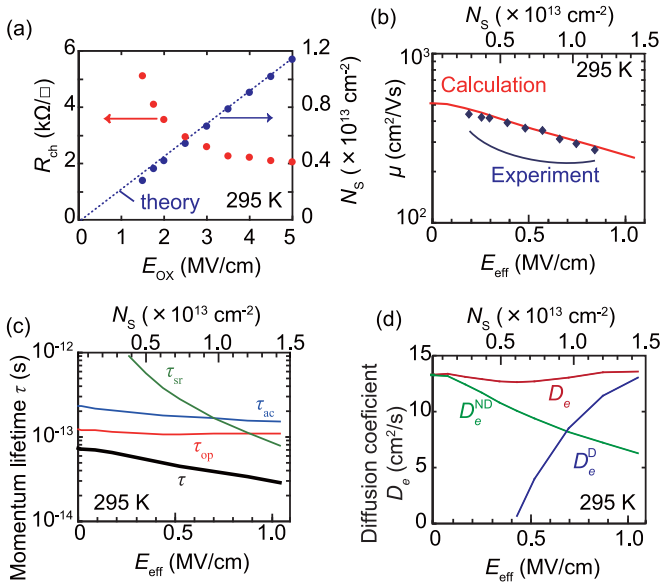

FIG. 2. (a) Channel sheet resistance R_{ch} (left axis) and sheet carrier (electron) density N_S (right axis) in the accumulation channel of Si, plotted as a function of the gate electric field $E_{ox} = V_{GS}/t_{BOX}$, which were estimated from a Hall measurement at 295 K. The red and blue circles are experimental R_{ch} and N_S results, respectively, and a blue dashed line represents a theoretical line of N_S estimated by $N_S = C_{ox}(V_{GS} - V_{fb})/q$. (b) Electron mobility μ plotted as a function of effective gate electric field $E_{eff} = q/\varepsilon_{Si}(N_S/2 - N_D t_{Si})$, which was estimated from Hall measurements at 295 K. The blue diamonds are the experimental results and the red solid curve is the fitting curve of a self-consistent calculation. In the figure, the N_S values are also shown in the upper axis. (c) Electron momentum lifetime τ as a function of E_{eff}, which were estimated by the self-consistent calculation: Total electron momentum lifetime τ (black line); momentum lifetime considering only optical phonon intervalley scattering, both f and g process τ_{op} (red line); acoustic phonon intravalley scattering τ_{ac} (blue line); and surface roughness scattering τ_{sr} (green line). In the figure, the N_S values are also shown in the upper axis. (d) Diffusion coefficient D_e plotted as a function of E_{eff}. The red, green, and blue curves are the curve estimated by Eq. (1d), $D_e^{ND} = k_B T \mu$, and $D_e^{D} = (E_F - E_0^{(2)})\mu$, respectively.

for the contact areas, which was used for the field isolation between contacts. Contact pads were formed by photolithography and etching with a $H_3PO_4 + H_2O$ solution, and the Hall bar structure was defined by photolithography and etching of the SiO_2 surface layer with BHF and the 15-nm-thick Si channel layer with Ar ion milling. After removal of the surface photoresist, finally a 100-nm-thick Al layer was deposited on the back side of the Si substrate for the back-gate contact.

In the electrical measurements at 295 K, a constant bias current I_{DS} and a constant gate-to-source voltage V_{GS} were applied, and the longitudinal voltage V_L and transverse voltages V_T were measured while a magnetic field was applied perpendicular to the substrate plane. The measurement configuration is also shown in Fig. 1. We estimated the channel sheet resistance R_{ch} and the sheet electron density N_S from V_L and V_T (Hall voltage), respectively. We applied V_{GS} from the back side of the p-Si substrate, and estimated the gate electric field E_{ox} by V_{GS}/t_{BOX}. Figure 2(a) shows R_{ch} and N_S as a function of E_{ox}, where red and blue circles are R_{ch} and N_S, respectively. In the same figure, the dashed line denoted by "theory" is the electron carrier density calculated by $N_S = C_{OX}(V_{GS} - V_{fb})/q$, where $C_{OX} = \varepsilon_{ox}/t_{BOX}$ is the gate capacitance, ε_{ox} is the permittivity of the BOX (SiO_2) layer, q is the elementary charge, $V_{fb} = qN_D t_{Si}/C_{OX} \sim 1.3$ V is the flat-band voltage, and $t_{Si} = 15$ nm is the Si channel thickness. Figure 1(a) shows good agreement in N_S between the experimental results and theoretical calculation (dashed line), confirming the reliability of the Hall measurement. Then, we estimated the electron mobility μ by the relation $\mu = \gamma_H/(qN_S R_{ch})$ under the assumption that the Hall factor $\gamma_H = 1$ [28], and also estimated the effective gate electric field $E_{eff} = q/\varepsilon_{Si}(N_S/2 - N_D t_{Si})$ acting on the V_{GS}-induced electrons, where ε_{Si} is the permittivity of Si [16]. Figure 2(b) shows μ plotted as a function of E_{eff}, where blue diamonds and a red curve represent the experimentally estimated mobility values and theoretical fitting that will be described in the next paragraph, respectively. The experimentally estimated values were 90% and 76% of the universal mobility [16] at $E_{eff} = 0.84$ and 0.19 MV/cm, respectively, in which a large mobility reduction in the lower field range probably comes from enhancement of both the acoustic and optical phonon scattering in the 15-nm-thick Si channel [26].

To estimate D_e and τ from the above-mentioned experimental results, we numerically calculated the 2D subband structure of the Si accumulation channel by solving the Poisson's and Schrödinger's equations self-consistently [19–27]. (A detailed procedure is described in Sec. S1 in the Supplemental Material (SM) [29]). We used ten subbands from the lowest energy level for the twofold (and fourfold) degenerated valleys at the conduction band minimum of Si (the total number of subbands is 20), and calculated the carrier distribution in each subband. In the calculation of τ, we took into account both the phonon scattering and surface roughness scattering. Following are the equations used to calculate D_e and τ [19–27,30–32]:

$$\tau = \sum_{v=2,4} \sum_{i=0-9} N_i^{(v)} \tau_i^{(v)} / N_S, \tag{1a}$$

$$\mu_i^{(v)} = \frac{q\tau_i^{(v)}}{m_c^{(v)}}, \tag{1b}$$

$$\mu = \sum_{v=2,4} \sum_{i=0-9} N_i^{(v)} \mu_i^{(v)} / N_S, \tag{1c}$$

$$D_e = \sum_{v=2,4} \sum_{i=0-9} N_i^{(v)} D_i^{(v)} / N_S, \tag{1d}$$

$$D_i^{(v)} = k_B T \mu_i^{(v)} \left[1 + \exp\left(-\frac{E_F - E_i^{(v)}}{k_B T} \right) \right] \times \ln\left[1 + \exp\left(\frac{E_F - E_i^{(v)}}{k_B T} \right) \right], \tag{1e}$$

$$\frac{1}{\tau_i^{(v)}(E)} = \frac{1}{\tau_{ac,i}^{(v)}(E)} + \frac{1}{\tau_{f,i}^{(v)}(E)} + \frac{1}{\tau_{g,i}^{(v)}(E)} + \frac{1}{\tau_{sr,i}^{(v)}(E)}, \tag{1f}$$

where k_B is Boltzmann's constant, $i = 0-9$ is the index for each subband, $v = 2$ and 4 express the twofold and fourfold degenerated valleys, respectively, $E_i^{(v)}$ is the energy, $N_i^{(v)}$ is the

sheet carrier density, $\tau_i^{(v)}$ is the energy-averaged momentum lifetime, $\mu_i^{(v)}$ is the mobility, and $m_c^{(v)}$ is the conduction effective mass of electrons in the ith subband of the v-fold valley. Equation (1e) is Einstein's relation for the 2D electron system [30–32]. For the electron scattering process, Eq. (1f) expresses Matthiessen's rule of the momentum lifetime for each scattering process; acoustic phonon intravalley scattering (τ_{ac}), optical phonon intervalley scattering (τ_{op}) including both f process ($\tau_{f,i}$) and g process ($\tau_{g,i}$), and surface roughness scattering (τ_{sr}). The scattering parameters used in the calculation of each lifetime, such as deformation potentials and a root-mean-square value of the Si/SiO_2 interface roughness, were determined so that the experimental mobility values [blue diamonds in Fig. 2(b)] are reproduced by Eq. (1c) [red line in Fig. 2(b)] [26]. These scattering parameters are listed in Table S2 in the SM [29].

Figure 2(c) shows the electron momentum lifetimes plotted as a function of E_{eff}, where black, blue, red, and green lines are the calculated results of τ, τ_{ac}, τ_{op}, and τ_{sr}, respectively. We can see that τ_{op} dominates τ in the lower field region ($E_{eff} \leqslant 0.8\,MV/cm$), whereas τ_{sr} dominates τ in the higher field region ($E_{eff} > 0.8\,MV/cm$). This result is consistent with the previous theoretical calculation on a 2D Si channel in a MOS structure [16]. Figure 2(d) shows D_e plotted as a function of E_{eff}, where the red line is the calculated result from Eq. (1d). We found that D_e is nearly independent of E_{eff}; as E_{eff} increases, D_e slightly decreases in the lower field range ($E_{eff} < 0.5\,MV/cm$) and slightly increases in the higher field range ($E_{eff} > 0.7\,MV/cm$). To clarify this trend, Einstein's relation for nondegenerated semiconductors $D_e^{ND} = k_B T \mu$ and that for 2D degenerated semiconductors $D_e^{D} = (E_F - E_0^{(2)})\mu$ are plotted in the same figure by the green line and the blue line, respectively, where $(E_F - E_0^{(2)})$ is the energy difference between the Fermi level and the zeroth subband of the twofold valley that is located at the lowest energy level [30–32]. As E_{eff} increases, D_e^{ND} decreases due to the decrease in the mobility μ but D_e^{D} increases due to the increase in the electron's Fermi energy. Thus, the accumulation channel is nondegenerated in the lower field range ($E_{eff} < 0.5\,MV/cm$) and degenerated in the higher field range ($E_{eff} > 0.7\,MV/cm$). In the later analysis, $R_{ch}(V_{GS})$ in Fig. 2(a) and $D_e(V_{GS})$ in Fig. 2(d) are used.

III. SPIN TRANSPORT IN SCHOTTKY-BARRIER (SB) SPIN MOSFETs

A. Device structure and measurement setup

Figures 3(a) and 3(b) show the side and top views of our SB spin-MOSFET structure, respectively, which has ferromagnetic source/drain (S/D) electrodes and reference electrodes (R1 and R2) located outside of the S and D electrodes, respectively. The device process is as follows. First, an SiO_2/SOI substrate was prepared using the same procedure as that for the Hall-bar-type MOSFET described in Sec. II. Using electron beam (EB) lithography, S, D, R1, and R2 contact areas on the SiO_2/SOI substrate were defined by opening contact holes on the EB resist on the top, and then the surface SiO_2 was etched with BHF so that the SiO_2 thickness of these areas became ~20 nm. After removing the EB resist, the substrate was cleaned by a $H_2SO_4 + H_2O_2$ solution, followed by

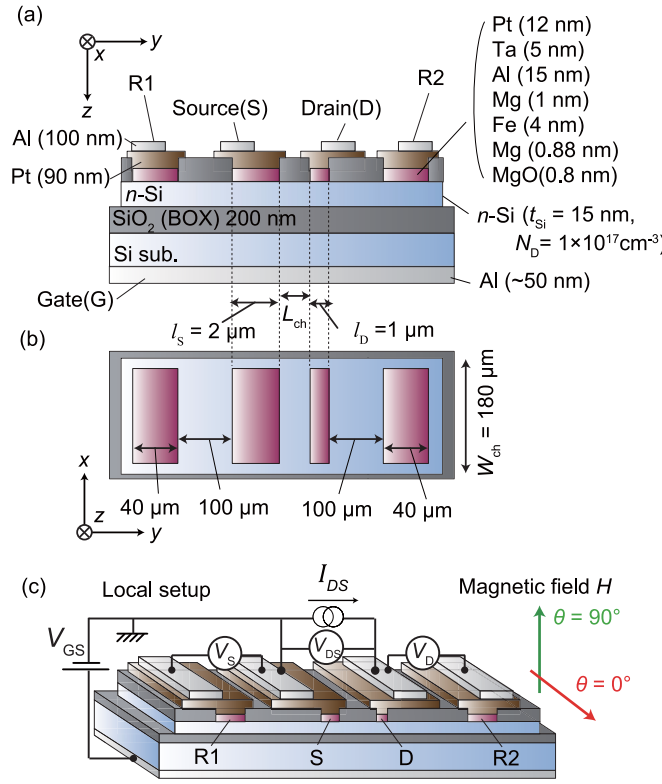

FIG. 3. (a) Side view and (b) top view of a SB spin MOSFET having Fe(4 nm)/Mg(0.88 nm)/MgO(0.8 nm)/Si Schottky-tunnel junctions prepared on a silicon-on-insulator (SOI) substrate, in which the thickness of the buried oxide (BOX) SiO_2 layer is 200 nm and the phosphorus donor doping concentration N_D of the 15-nm-thick Si channel is $1 \times 10^{17}\,cm^{-3}$. The Cartesian coordinate is defined as follows: x and y are parallel to the long and short sides of the electrodes, respectively, and z is normal to the substrate plane. The channel length L_{ch} along the y direction and width W_{ch} along the x direction are defined, and the short side lengths along the y direction of the source (S) and drain (D) electrodes are $l_S = 2\,\mu m$ and $l_D = 1\,\mu m$, respectively. R1 and R2 are located at ~100 μm away from the S and D electrodes, respectively, and their short side lengths along the y direction are 40 μm. (c) Local measurement setup of the SB spin MOSFET, where the voltage between the R1/S, S/D, and D/R2 electrodes are measured simultaneously by voltage meters V_S, V_{DS}, and V_D, respectively, while a constant current I_{DS} is driven between the D and S electrodes and a constant gate voltage V_{GS} is applied between the back contact and the S electrode. In the measurements, an external magnetic field is applied along the plane ($\theta = 0°$, along the $-x$ direction) or perpendicular to the plane ($\theta = 90°$, along the $-z$ direction) and it is swept between −3000 and 3000 Oe.

flowing DI water. Then, the Si surface of the contact areas was opened by dipping the whole substrate into BHF. Immediately after drying with a N_2 gas blow, the substrate was installed into an ultrahigh vacuum system, and (from top to bottom) an Al(15 nm)/Mg(1 nm)/Fe(4 nm)/Mg(0.88 nm)/MgO(0.8 nm) layered structure was successively deposited at room temperature by molecular beam epitaxy (MBE) and EB evaporation. Immediately after being exposed to air, a Pt(12 nm)/Ta(5 nm) cap layer was deposited on the surface. Then, the lateral structures of S, D, R1, and R2 electrodes were defined by Ar ion etching with an EB resist mask on the top of each

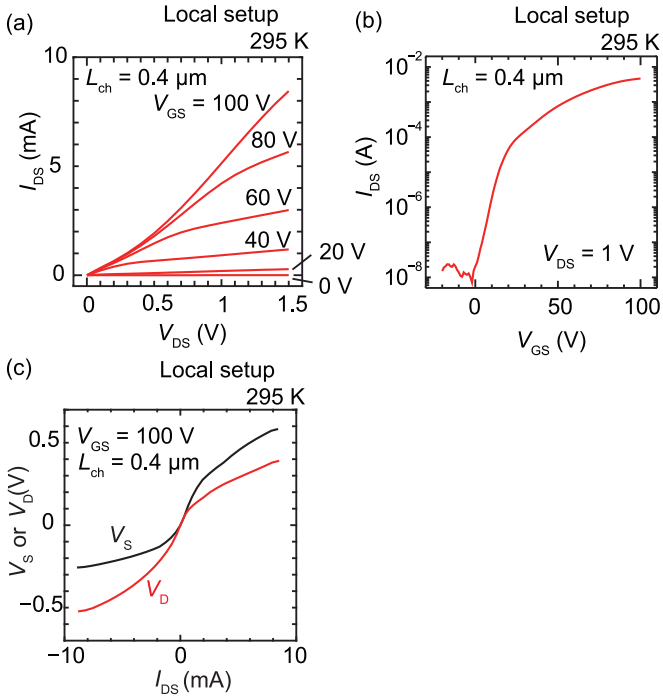

FIG. 4. (a) I_{DS}-V_{DS} characteristics measured at 295 K for a SB spin MOSFET with $L_{ch} = 0.4\,\mu$m, where V_{GS} was varied from 0 to 100 V in 20-V steps. (b) I_{DS}-V_{GS} characteristics measured at 295 K for the same device, where $V_{DS} = 1$ V. (c) V_S-I_{DS} (black solid curve) and V_D-I_{DS} (red solid curve) plots measured at 295 K for the same device, where $V_{GS} = 100$ V.

electrode. After removing the EB resist, electrode extensions attached to the top of the S, D, R1, and R2 electrodes were fabricated using a sputter-deposited Pt(90 nm)/Ta(5 nm) layer, EB lithography, and Ar ion etching, and then a 100-nm-thick Al pad was formed on each electrode extension using photolithography, thermal evaporation, and lift-off process. Then, a 50-nm-thick Al layer was deposited on the back side of the substrate for the back-gate contact after removing the surface native oxide. Finally, each device was isolated by a square-shaped island structure using photolithography, BHF etching of the surface SiO_2 layer, and Ar ion etching of the 15-nm-thick Si channel layer. The structural parameters defined in Figs. 3(a) and 3(b) are as follows: The channel lengths L_{ch} along the y axis are 0.3, 0.4, 0.5, 1.0, 2.0, 5.0, and 10 μm, the channel width W_{ch} along the x axis is 180 μm, the distance between the S and R1 (D and R2) electrodes along the y axis is ~100 μm, the lengths of the S electrode l_S and the D electrode l_D along the y axis are 2 and 1 μm, respectively, and the lengths of the R1 and R2 electrodes along the y axis are 40 μm. Our device structure has a Si channel with a constant $N_D = 1 \times 10^{17}$ cm^{-3}, which is different from the previously reported spin MOSFET that has highly doped Si regions ($N_D \sim 1 \times 10^{20}$ cm^{-3}) under S/D contacts [11]. One advantage of our device structure is to eliminate strong spin scattering in such a highly doped Si region.

Figure 3(c) shows our measurement setup for the two-terminal (2T) spin transport signals, where the voltages (V_{DS}, V_D, and V_S) between the two electrodes are measured while a constant current I_{DS} is driven from the D to the S electrodes through the Si channel and a magnetic field H is applied along an in-plane direction ($\theta = 0°$, the $-x$ direction) or the perpendicular direction ($\theta = 90°$, the $-z$ direction). V_{DS} is the voltage between the D and S electrodes, which is the total voltage drop through the Si channel, and V_D (V_S) is the voltage between D and R2 (between S and R1), which is the junction voltage drop at the drain (source) junction including the MgO tunnel barrier and the Schottky barrier at the surface of the Si channel. Figures 4(a) and 4(b) show I_{DS}-V_{DS} and I_{DS}-V_{GS} characteristics measured at 295 K for a device with $L_{ch} = 0.4\,\mu$m, respectively. We observed clear transistor operations with a high on/off ratio ~10^6. Figure 4(c) shows V_S-I_{DS} (black solid curve) and V_D-I_{DS} (red solid curve) plots of the same device at 295 K, where $V_{GS} = 100$ V. Here, $|V_S|$ at $I_{DS} = 5$ mA is larger than that at $I_{DS} = -5$ mA because the reverse-biased Schottky barrier is formed under the S electrode when I_{DS} is positive. On the contrary, $|V_D|$ at $I_{DS} = 5$ mA is smaller than that at $I_{DS} = -5$ mA because the forward-biased Schottky barrier is formed under the D electrode when I_{DS} is positive. When $I_{DS} = 5$ mA and $V_{GS} = 100$ V, V_S, V_D, and V_{DS} are 0.45, 0.23, and 0.93 V, respectively.

B. Spin-valve signals measured with $V_{GS} = 100$ V

Figures 5(a)–5(c) show the voltage changes ΔV_D, ΔV_S, and ΔV_{DS}, respectively, as a function of magnetic field, measured at 295 K for a device with $L_{ch} = 0.4\,\mu$m, where the

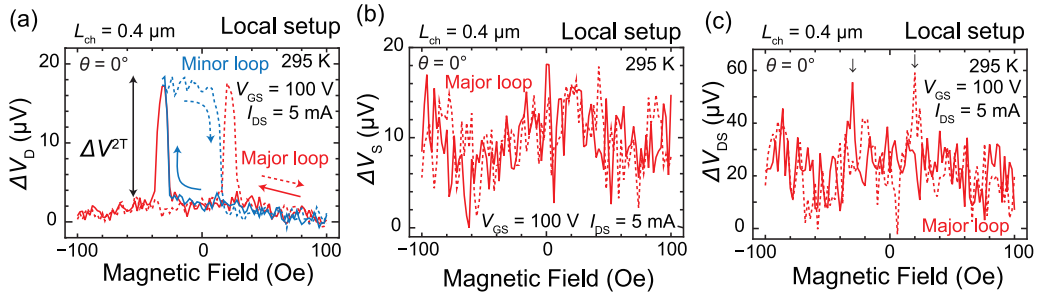

FIG. 5. (a–c) Voltage change (a) ΔV_D, (b) ΔV_S, and (c) ΔV_{DS} measured at 295 K with $I_{DS} = 5$ mA and $V_{GS} = 100$ V for a SB spin MOSFET with $L_{ch} = 0.4\,\mu$m, while an in-plane magnetic field ($\theta = 0°$) is swept. The red solid (dashed) curves are major loops measured with a magnetic field swept from the positive to negative direction (from the negative to positive direction). In (a), the blue solid (dashed) curve is a minor loop measured with a magnetic field swept from the positive to negative direction (from the negative to positive direction). ΔV^{2T} represents the amplitude of the spin-valve signal. In (c), the two vertical arrows indicate the signal peaks at −30 and 20 Oe.

measurement parameters are $I_{DS} = 5\,\text{mA}$ and $V_{GS} = 100\,\text{V}$, and the magnetic field is applied in the film plane along the $-x$ direction ($\theta = 0^\circ$). In Fig. 5(a), the major loop of ΔV_D represented by solid and dashed red curves shows a clear spin-valve signal with two peaks at -30 and $+20$ Oe, which originates from the parallel and antiparallel magnetization configurations of the Fe layers in the S and D electrodes. The minor loop represented by solid and dashed blue curves also indicates that the result of Fig. 5(a) is caused by the spin-valve effect, which reflects the magnetization reversal of the Fe layer in the S electrode. Thus, this means that spin-polarized electrons injected from the S electrode transport through the Si 2D electron accumulation channel and finally they are detected by the D electrode; namely, the spin-dependent transport in the spin MOSFET was demonstrated at 295 K. Since the total resistance between the S and D electrodes is 186 Ω and the change in resistance is 2.9 mΩ, the MR ratio of the device is 0.003%, which is smaller by a factor of 10 than that in a previous report by another group [11]. This comes from the fact that the total resistance of our device is higher than that in the previous report, since the uniform donor doping with $N_D = 1 \times 10^{17}\,\text{cm}^{-3}$ in the channel leads to high Schottky-barrier resistances under the S and D electrodes.

In Fig. 5(c), the major loop of ΔV_{DS} represented by solid and dashed red curves is noisy compared with that of ΔV_D in Fig. 5(a), but it has clear two peaks at -30 and $+20$ Oe which are denoted by vertical arrows. Since these peak positions are identical with those in the clear spin-valve signal of ΔV_D in Fig. 5(a), the major loop of ΔV_{DS} reflects the spin-valve signal. On the other hand, in Fig. 5(b), the major loop of ΔV_S represented by solid and dashed red curves does not have apparent peaks as those in Figs. 5(a) and 5(c). This is because the spin-valve signal is not detectable in ΔV_S due to the high electrical field of the reverse-biased Schottky junction under the S electrode [4,11,33,34]. (Details are shown in Sec. S4 in the SM [29]). For the same reason, a so-called nonlocal signal [5] is not detectable in our device (details are shown in Sec. S5 in the SM [29]). Note that the signal fluctuation in ΔV_S and ΔV_{DS} probably comes from the thermal noise of the reverse-biased Schottky junction under the S electrode.

We also measured the Hanle signal with a perpendicular magnetic field ($\theta = 90^\circ$) to confirm the spin transport through the 2D accumulation channel (details are shown in Secs. S2 and S3 in the SM [29]). We found that ΔV_D is composed of a negative Hanle signal at around zero magnetic field and a positive broader background signal in the whole magnetic field range [4,35–37]. Since the amplitude of the Hanle signal was almost half of the spin-valve signal amplitude, we confirmed again that the spin-valve signal in Fig. 5(a) originates from the spin transport from the S to D electrodes through the Si channel in our device. Hence, the SB spin MOSFET operation at room temperature is demonstrated.

C. Analysis of the V_{GS}-dependent spin diffusion length λ_S obtained from the spin-valve signals measured for various channel lengths L_{ch}

To obtain the electron spin diffusion length λ_S at various gate electric fields $E_{ox} = V_{GS}/t_{BOX}$, we measured ΔV_D for devices with various L_{ch} (= 0.3, 0.4, 0.5, 1.0, 2.0, 5.0, and 10 μm) under various V_{GS} (= 40, 50, 60, 80, and 100 V) and a sweeping in-plane magnetic field ($\theta = 0^\circ$), and analyzed the amplitude of the spin-valve signal ΔV^{2T} defined in Fig. 5(a). In the measurements, I_{DS} values were not exactly the same in all the devices and in all the V_{GS} values, because both the channel resistance and S/D junction resistances are dramatically changed by V_{GS}. Since ΔV^{2T} was almost proportional to I_{DS}, resistance change $\Delta R = \Delta V^{2T}/I_{DS}$ was used in our analysis.

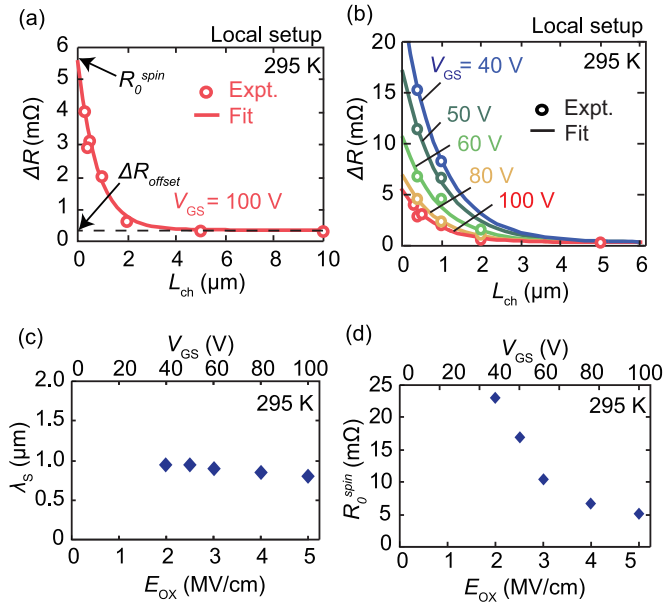

FIG. 6. (a) Resistance change $\Delta R = \Delta V^{2T}/I_{DS}$ plotted as a function of channel length L_{ch}, where measurements were performed at 295 K with $V_{GS} = 100\,\text{V}$. The open circles are experimental values, the solid line is the fitting result by Eq. (4a), and the dashed line is the offset resistance change ΔR_{offset}. (b) ΔR plotted as a function of L_{ch}, where blue, dark green, light green, orange, and red open circles are experimental values for $V_{GS} = 40$, 50, 60, 80, and 100 V, respectively, and blue, dark green, light green, orange, and red curves are the fitting curves for the experimental values with the same color. (c) Spin diffusion length λ_S and (d) R_0^{spin} plotted by blue diamonds as a function of gate electric field $E_{ox} = V_{GS}/t_{BOX}$, where those values were estimated from the fitting results in (b). The V_{GS} values are also shown in the upper axis.

In all the devices with different L_{ch}, clear spin-valve signals similar to those in Fig. 5(a) were observed under $V_{GS} = 100\,\text{V}$, which allows us to obtain ΔV^{2T}. Figure 6(a) shows ΔR plotted as a function of L_{ch}, where red open circles are experimental values and a red curve is the fitting curve that will be described later. As L_{ch} increases from $L_{ch} = 0.3\,\mu$m, ΔR exponentially decreases and then shows a constant value ΔR_{offset} at $L_{ch} \geqslant 5\,\mu$m, which is denoted by a black dashed line. Considering that λ_S is likely to be smaller than 5 μm, the constant ΔR ($=\Delta R_{offset}$) at $L_{ch} \geqslant 5\,\mu$m is the signal change in a parasitic magnetoresistance which probably originates from tunneling anisotropic magnetoresistance (TAMR) [4,38] in the Fe/Mg/MgO/Si junction at the D electrode.

To estimate the spin injection/detection polarization P_S and λ_S, we derived an analytical expression for the spin-valve signals through a Si 2D accumulation channel. The following equation is the analytical expression of the spin-valve signal in a lateral device having a thin channel ($t_{ch} \ll \lambda_S$) and the short

electrode lengths of the S/D electrodes (l_S, $l_D \ll \lambda_S$) [4];

$$\Delta V^{2T} = {P_S}^2 \frac{\rho_{ch}}{W_{ch} t_{ch}} I_{DS} \lambda_S \exp\left(-\frac{L_{ch}}{\lambda_S}\right), \quad (2)$$

where t_{ch} is the channel thickness, and ρ_{ch} is the channel resistivity. Here, we assume that the lateral electric field in the channel is small and the spin drift effect [33,39] is negligible. The term $\rho_{ch}/(W_{ch}t_{ch})$ represents the channel resistivity per unit length along the spin transport direction. In the case of a 2D electron accumulation channel, $\rho_{ch}/(W_{ch}t_{ch})$ should be replaced by R_{ch}/W_{ch}:

$$\Delta V^{2T} = {P_S}^2 \frac{R_{ch}}{W_{ch}} I_{DS} \lambda_S \exp\left(-\frac{L_{ch}}{\lambda_S}\right), \quad (3)$$

where R_{ch} is the sheet resistance [$\Omega/\square$] of the accumulation channel.

Based on Eq. (3), we fit the following formula to the experimental values:

$$\Delta R = R_0^{spin} \exp\left(-\frac{L_{ch}}{\lambda_S}\right) + \Delta R_{offset}, \quad (4a)$$

$$R_0^{spin} = {P_S}^2 \frac{R_{ch}}{W_{ch}} \lambda_S, \quad (4b)$$

where R_0^{spin} is the effective spin resistance in the accumulation channel taking into account P_S, and ΔR_{offset} is the amplitude of the parasitic MR independent of L_{ch}. From the fitting curve in Fig. 6(a), we obtained $R_0^{spin} = 5.2\,\mathrm{m\Omega}$, $\lambda_S = 0.8\,\mu\mathrm{m}$, and $\Delta R_{ofset} = 0.35\,\mathrm{m\Omega}$ at $V_{GS} = 100\,\mathrm{V}$. It should be noted that the condition l_S, $l_D \ll \lambda_S$ assumed in Eq. (2) is not satisfied in our device structure ($l_S = 2\,\mu\mathrm{m}$ and $l_D = 1\,\mu\mathrm{m}$). Thus, the R_0^{spin} value estimated with Eq. (4b) is the lower bound value, since the spin-valve signal becomes smaller with increasing l_S, $l_D (> \lambda_S)$ by the electrode averaging effect (EAE) [4,40]. On the other hand, the λ_S values estimated by this procedure is accurate, since the term $\exp(-L_{ch}/\lambda_S)$ in Eq. (4a) remains unchanged even in the condition of l_S, $l_D > \lambda_S$ [4].

In the same manner, we estimated ΔR for the devices with L_{ch} (= 0.4, 1.0, 2.0, 5.0 and 10 μm) under various V_{GS} (= 40, 50, 60, and 80 V), and plotted them as a function of L_{ch}, and finally estimated R_0^{spin}, λ_S, and ΔR_{ofset} for each V_{GS} by fitting Eq. (4a). Figure 6(b) shows ΔR plotted as a function of L_{ch}, where blue, dark green, light green, orange, and red open circles are experimental values for $V_{GS} = 40$, 50, 60, 80, and 100 V, respectively, and blue, dark green, light green, orange, and red curves are the fitting curves for the experimental values with the same color. In all the plots, the experimental ΔR values for each V_{GS} show an exponential decrease with increasing L_{ch} and a constant value in the higher L_{ch} range. We see very good agreement between the experimental values and fitting curves. Figure 6(c) shows λ_S plotted as a function of $E_{ox} = V_{GS}/t_{BOX}$, in which λ_S is 0.95 μm at $E_{ox} = 2.0$ MV/cm ($E_{eff} = 0.35$ MV/cm) and slightly decreases with increasing V_{GS}, and it is 0.80 μm at $E_{ox} = 5.0$ MV/cm ($E_{eff} = 0.88$ MV/cm). This result is comparable to the value in a previous report: $\lambda_S = 0.85\,\mu\mathrm{m}$ at $E_{ox} = 2.5\,\mathrm{MV/cm}$ [11]. Figure 6(d) shows R_0^{spin} plotted as a function of E_{ox}, in which R_0^{spin} rapidly decreases with increasing E_{ox}. This feature probably comes from the decrease in R_{ch} with increasing E_{ox} as shown in Fig. 2(a) and almost constant λ_S as shown in Fig. 6(c), since R_0^{spin} is proportional to R_{ch} and λ_S in Eq. (4b).

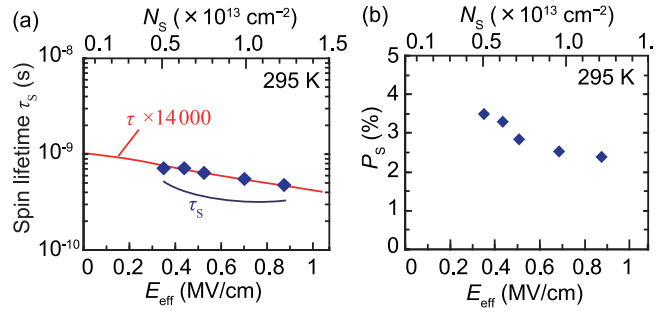

FIG. 7. (a) Spin lifetime τ_S in the 2D accumulation channel plotted as a function of effective gate electric field E_{eff}, where blue diamonds are estimated values. The red line is τ in Fig. 2(c) multiplied by 14 000. The N_S values are also shown in the upper axis. (b) Spin polarization P_S plotted as a function of E_{eff}, where blue diamonds are estimated values by Eq. (4b). The N_S values are also shown in the upper axis.

IV. RELATION BETWEEN THE ELECTRON SPIN LIFETIME τ_S AND MOMENTUM LIFETIME τ

We estimated τ_S at each V_{GS} using the relationship ${\lambda_S}^2 = D_e \tau_S$, D_e in Fig. 2(d), and λ_S in Fig. 6(c). Figure 7(a) shows τ_S plotted as a function of the effective gate electric field $E_{eff} = q/\varepsilon_{Si}(N_S/2 - N_D t_{Si})$, where blue diamonds are τ_S values estimated here. The τ_S value at each E_{eff} is consistent with the linewidth of the Hanle signal measured with the same E_{eff} (see Secs. S2 and S3 in the SM [29]), and all the values are comparable to ~1 ns that was obtained in a Si 2D electron inversion channel [12]. From the semilog plot in Fig. 7(a), τ_S is 0.71 ns at $E_{eff} = 0.35\,\mathrm{MV/cm}$, it decreases monotonically with increasing E_{eff}, and it is 0.47 ns at $E_{eff} = 0.88\,\mathrm{MV/cm}$, which is very similar to the feature of τ vs E_{eff} in Fig. 2(c). Based on this result, the τ values were multiplied by 14 000 and plotted as a red line in Fig. 7(a). We found that the value $\tau \times 14\,000$ and τ_S are almost identical in the E_{eff} range examined in this study (0.35–0.88 MV/cm). This result means that the spin-flip rate per one momentum scattering event $\tau/\tau_S \sim 1/14\,000$ is almost constant.

Figure 7(b) shows P_S plotted as a function of E_{eff}, which were estimated using R_{ch} in Fig. 2(a), R_0^{spin} in Fig. 6(d), and Eq. (4b). As E_{eff} increases from 0.35 to 0.88 MV/cm, P_S decreases from 3.5% to 2.5%. The almost constant P_S indicates that E_{ox} dependences of R_0^{spin} and R_{ch} are similar to each other, as mentioned in Sec. III.

V. DISCUSSION

In the preceding sections, we obtained the result that τ/τ_S is almost constant at ~1/14 000 in the Si 2D electron accumulation channel in our SB spin MOSFETs, even when the dominant scattering process in the total electron momentum scattering is changed from the phonon scattering to the surface roughness scattering by increasing E_{eff}, as analyzed in Sec. II. Spin relaxation in the semiconductor with an inversion symmetry is discussed by the Elliott-Yafet (EY) mechanism

that predicts a proportional relation between τ and τ_S [13–15]:

$$\frac{\tau}{\tau_S} \sim (\Delta g)^2, \tag{5}$$

where $\Delta g \equiv 2.0023 - g$ is the shift of the g factor which is associated with the strength of the spin-orbit coupling (SOC). The almost constant τ/τ_S indicates that the EY mechanism dominates the spin relaxation in the accumulation channel, and that the strength of SOC during both phonon scattering and surface roughness scattering are the same. On the other hand, the spin-orbit interaction can arise at a Si/oxide interface due to the break of the structural inversion symmetry [41], and its strength theoretically increases with increasing the gate electric field. Since the τ/τ_S value is almost independent of $E_{\rm eff}$ examined in this study (0.35–0.88 MV/cm), such influence of the spin-orbit interaction was not observed in our spin MOSFETs.

In the following, we discuss the τ/τ_S value assuming that the spin relaxation is dominated by the EY mechanism. From the value obtained in the previous ESR measurement on a bulk Si material [42,43] and Eq. (5), $\tau/\tau_S = 1/45\,000 - 1/77\,000$ is estimated for the phosphorus doping concentration $N_D = 1 \times 10^{17}\,{\rm cm}^{-3}$ which is the same as that of the channel in our spin MOSFETs. These τ/τ_S values are smaller by a factor of 4 than our result $\tau/\tau_S \sim 1/14\,000$. This leads to the conclusion that the SOC in the 2D accumulation channel is almost twice as strong as that in the bulk Si material when we assumes Δg in Eq. (5) is simply proportional to the SOC strength. Considering the absence of $E_{\rm eff}$ dependence in τ/τ_S, this increase is possibly caused by fixed charges near the Si/SiO_2 interface, such as charged interface defects.

To realize large spin-valve signals, it is required to reduce the number of the spin scattering events during the electron transport through a 2D accumulation channel of Si. There are two candidate methods for this purpose. The first method is to enhance τ. Under the condition that τ/τ_S is unchanged, the number of spin scattering events decreases as τ increases. The second method is to reduce the spin-flip rate per one momentum scattering event, τ/τ_S. To increase τ, the technologies established in ordinary MOSFETs can be applied. In Ref. [17], a theoretical study predicts that both methods are possible when an in-plane biaxial tensile strain is introduced into a Si channel that is thin enough to generate a subband structure; by introducing 1% in-plane biaxial strain, τ is increased by a factor of 2, whereas τ/τ_S is reduced by three orders of magnitude due to the increase of the energy difference between the lowest subband energy of twofold valley $E_0^{(2)}$ and fourfold valley $E_0^{(4)}$. At present, however, it is unclear whether the reduction of τ/τ_S is possible or not, since the underlying physics for the relation between τ_S and τ has not been experimentally clarified. This is an open question to be studied in the future. To deeply understand the spin scattering mechanism in a 2D accumulation/inversion channel of Si, further experimental investigations with different channel properties are strongly needed.

VI. CONCLUSION

We have investigated Schottky-barrier (SB) spin MOSFETs having Fe/Mg/MgO/Si Schottky-tunnel junctions at the source/drain contacts and a 15-nm-thick nondegenerated Si channel with a phosphorus donor doping concentration N_D of $1 \times 10^{17}\,{\rm cm}^{-3}$. The spin MOSFETs with various channel lengths ($L_{\rm ch} = 0.3-10\,\mu$m) exhibit accumulation-mode transistor characteristics with the high on/off ratio of $\sim 10^6$ as well as the clear spin-valve signals at 295 K. Although the spin-valve signal (MR ratio) is small, we showed spin-MOSFET operation at room temperature.

In preparation for the quantitative analyses of the spin-dependent electron transport properties through the Si two-dimensional (2D) electron accumulation channel, we first estimated the electron momentum lifetime τ and diffusion coefficient D_e in the Si 2D electron accumulation channel with various gate electric fields. We used the experimental results obtained from a Hall-bar-type device and self-consistent calculations with Poisson's and Schrödinger's equations. Then, we observed spin-valve signals measured in an effective gate electric field $E_{\rm eff}$ range of 0.35–0.88 MV/cm for various channel lengths. By analyzing the experimental data with the theoretical model, we have obtained the following important results:

(I) The spin diffusion length λ_S is 0.95 μm at $E_{\rm eff} = 0.35$ MV/cm, it decreases monotonically with increasing $E_{\rm eff}$, and it is 0.80 at $E_{\rm eff} = 0.88$ MV/cm.

(II) The spin lifetime τ_S is 0.71 ns at $E_{\rm eff} = 0.35$ MV/cm, it decreases monotonically with increasing $E_{\rm eff}$, and it is 0.47 ns at $E_{\rm eff} = 0.88$ MV/cm.

(III) The spin-flip rate per one momentum scattering event τ/τ_S is $\sim 1/14\,000$ and it is almost unchanged by $E_{\rm eff}$, while the dominant momentum scattering process is changed from the phonon scattering to the surface roughness scattering with increasing $E_{\rm eff}$.

From the result (III), we concluded that the Elliott-Yafet mechanism [13–15] dominates the spin relaxation in the Si 2D electron accumulation channel, and that the spin-flip rate per one phonon scattering event and surface roughness scattering event are the same. Based on the Elliott-Yafet mechanism, however, the τ/τ_S values estimated from the previous ESR measurements [42,43] for the bulk Si material with the same doping concentration $N_D \sim 1 \times 10^{17}\,{\rm cm}^{-3}$ are smaller by a factor of 4 than our result $\tau/\tau_S \sim 1/14\,000$. Therefore, there is a possibility that the spin-orbit coupling in the Si 2D electron accumulation channel is almost twice as strong as that in bulk Si materials.

To realize large spin-valve signals, it is required to reduce the number of spin scattering events during the electron transport through a 2D accumulation channel of Si. For this purpose, we addressed two possible methods to change the scattering parameters τ and τ/τ_S. To establish such channel engineering, it is mandatory to deeply understand the spin scattering mechanism in Si 2D accumulation/inversion channels, and further experimental investigations with different channel properties are strongly needed.

ACKNOWLEDGMENTS

This work was partially supported by Grants-in-Aid for Scientific Research (Grants No. 16H02095 and No. 18H05345), CREST of JST (Grant No. JPMJCR1777), Yazaki Science and Technology Foundation, and Spintronics Research Network of Japan.

[1] S. Sugahara and M. Tanaka, Appl. Phys. Lett. **84**, 2307 (2004).
[2] S. Sugahara and M. Tanaka, ACM Trans. Storage **2**, 197 (2006).
[3] M. Tanaka and S. Sugahara, IEEE Trans. Electron Devices **54**, 961 (2007).
[4] S. Sato, R. Nakane, T. Hada, and M. Tanaka, Phys. Rev. B **96**, 235204 (2017).
[5] T. Suzuki, T. Sasaki, T. Oikawa, M. Shiraishi, Y. Suzuki, and K. Noguchi, Appl. Phys. Express **4**, 023003 (2011).
[6] M. Ishikawa, H. Sugiyama, T. Inokuchi, T. Tanamoto, K. Hamaya, N. Tezuka, and Y. Saito, J. Appl. Phys. **114**, 243904 (2013).
[7] R. Nakane, T. Harada, K. Sugiura, and M. Tanaka, Jpn. J. Appl. Phys. **49**, 113001 (2010).
[8] H.-J. Jang and I. Appelbaum, Phys. Rev. Lett. **103**, 117202 (2009).
[9] T. Tahara, H. Koike, M. Kameno, S. Sasaki, Y. Ando, K. Tanaka, S. Miwa, Y. Suzuki, and M. Shiraishi, Appl. Phys. Express **8**, 113004 (2015).
[10] M. Kameno, Y. Ando, T. Shinjo, H. Koike, T. Sasaki, T. Oikawa, T. Suzuki, and M. Shiraishi, Appl. Phys. Lett. **104**, 092409 (2016).
[11] T. Sasaki, Y. Ando, M. Kameno, T. Tahara, H. Koike, T. Oikawa, T. Suzuki, and M. Shiraishi, Phys. Rev. Appl. **2**, 034005 (2014).
[12] J. Li and I. Appelbaum, Phys. Rev. B **84**, 165318 (2011).
[13] R. J. Elliott, Phys. Rev. **96**, 266 (1954).
[14] G. Lancaster, J. A. van Wyk, and E. E. Schneider, Proc. Phys. Soc., London **84**, 19 (1964).
[15] P. Boross, B. Dóra, A. Kiss, and F. Simon, Sci. Rep. **3**, 3233 (2013).
[16] S. Takagi, A. Toriumi, M. Iwase, and H. Tango, IEEE Trans. Electron Devices **41**, 2363 (1994).
[17] D. Osintsev, V. Sverdlov, and S. Selberherr, *Progress in Industrial Mathematics at ECMI, 2014*, edited by G. Russo, V. Capasso, and V. Romano (Springer International Publishing AG, Gewerbestrasse, Switzerland, 2016), p. 695.
[18] V. Sverdlov and S. Selberherr, Phys. Rep. **585**, 1 (2015).
[19] F. Stern, J. Comput. Phys. **6**, 56 (1970).
[20] F. Stern, Phys. Rev. B **5**, 4891 (1972).
[21] T. Ando, A. B. Fowler, and F. Stern, Rev. Mod. Phys **54**, 437 (1982).
[22] B. K. Ridley, J. Phys. C: Solid State Phys. **15**, 5899 (1982).
[23] K. Masaki, C. Hamaguchi, K. Taniguchi, and M. Iwase, Jpn. J. Appl. Phys. **28**, 1856 (1989).
[24] K. Masaki, Ph.D. thesis, Osaka University, 1992.
[25] S. Takagi, J. L. Hoyt, J. J. Weiser, and J. F. Gibbons, J. Appl. Phys. **80**, 1567 (1996).
[26] S. Takagi, J. Koga, and A. Toriumi, Jpn. J. Appl. Phys. **37**, 1289 (1998).
[27] C. Hamaguchi, *Basic Semiconductor Physics*, 2nd ed. (Springer-Verlag, Berlin, Germany, 2010), p. 340.
[28] S. Kobayashi, M. Saitoh, Y. Nakabayshi, T. Ishihara, T. Numata, and K. Uchida, Jpn. J. Appl. Phys. **49**, 04DC23 (2010).
[29] See Supplemental Material at http://link.aps.org/supplemental/10.1103/PhysRevB.99.165301 for (S1) self-consistent calculation of a two-dimensional electron accumulation channel in the Si layer in the vicinity of the BOX (SiO_2) layer, (S2) Hanle signals observed in the SB spin MOSFET, (S3) spin extraction/detection via a forward-biased Schottky barrier, (S4) spin injection/detection via a reverse-biased Schottky barrier, and (S5) spin detection via a Schottky barrier in the nonlocal measurement setup, which includes Refs. [44–50].
[30] D. Tjapkin, V. Milanović, and Ž. Spasojaveć, Phys. Status Solidi A **63**, 737 (1981).
[31] D. R. Choudhury, P. K. Bash, and A. N. Chakravariti, Phys. Status Solidi A **38**, K85 (1976).
[32] A. H. Marshak and D. Assaf III, Solid State Electron. **16**, 675 (1973).
[33] M. Kameno, Y. Ando, E. Shikoh, T. Shinjo, T. Sasaki, T. Oikawa, Y. Suzuki, T. Suzuki, and M. Shiraishi, Appl. Phys. Lett. **101**, 122413 (2012).
[34] S. Sato, R. Nakane, T. Hada, and M. Tanaka, Phys. Rev. B **97**, 199901(E) (2018).
[35] Y. Aoki, M. Kameno, Y. Ando, E. Shikoh, Y. Suzuki, T. Shinjo, M. Shiraishi, T. Sasaki, T. Oikawa, and T. Suzuki, Phys. Rev. B **86**, 081201 (2012).
[36] S. Sato, R. Nakane, and M. Tanaka, Appl. Phys. Lett. **107**, 032407 (2015).
[37] O. Txoperena and F. Casanova, J. Phys. D: Appl. Phys. **49**, 133001 (2016).
[38] S. Sharma, S. P. Dash, H. Saito, S. Yuasa, B. J. van Wees, and R. Jansen, Phys. Rev. B **86**, 165308 (2012).
[39] Z. G. Yu and M. E. Flatté, Phys. Rev. B **66**, 235302 (2002).
[40] Y. Takamura, T. Akushichi, Y. Shuto, and S. Sugahara, J. Appl. Phys. **117**, 17D919 (2015).
[41] M. Prada, G. Klimeck, and R. Joynt, New J. Phys. **13**, 013009 (2011).
[42] I. Gränacher and W. Czaja, J. Phys. Chem. Solids **28**, 231 (1967).
[43] H. Kodera, J. Phys. Soc. Jpn. **21**, 1040 (1966).
[44] F. J. Jedema, H. B. Heersche, A. T. Filip, J. J. A. Baselmans, and B. J. Van Wees, Nature (London) **416**, 713 (2002).
[45] X. Lou, C. Adelmann, M. Furis, S. A. Crooker, C. J. Palmstrøm, and P. A. Crowell, Phys. Rev. Lett. **96**, 176603 (2006).
[46] T. Valet and A. Fert, Phys. Rev. B **48**, 7099 (1993).
[47] A. Fert and H. Jaffrès, Phys. Rev. B **64**, 184420 (2001).
[48] M. Julliere, Phys. Lett. A **54**, 225 (1975).
[49] E. H. Rhoderick, *Metal-Semiconductor Contacts*, edited by P. Hammond and D. Walsh (Oxford University Press, Oxford, UK, 1978).
[50] F. J. Jedema, M. V. Costache, H. B. Heersche, J. J. A. Baselmans, and B. J. van Wees, Appl. Phys. Lett. **81**, 5162 (2002).